Heterojunction plasmonic midinfrared detectors

2 authors:

Manmohan Shishodia
Gautam Buddha University
31 PUBLICATIONS   **123** CITATIONS

SEE PROFILE

A. G. U. Perera
Georgia State University
330 PUBLICATIONS   **3,624** CITATIONS

SEE PROFILE

Some of the authors of this publication are also working on these related projects:

Scattering and Far/Near Field Characteristics of Metallic Nanoparticles for Photovoltaic Applications View project

The development of efficient theoretical and simulation tools for developing low cost and high figure of merit plasmonic sensors based on isolated and coupled nanoparticle systems View project

Heterojunction plasmonic midinfrared detectors

M. S. Shishodia and A. G. Unil Perera[a]
Department of Physics and Astronomy, Georgia State University, Atlanta, Georgia 30303, USA

In view of the emergence of wide ranging applications in the areas such as environmental monitoring, medical diagnostics, defense, security and sensing etc., it is indispensable to develop resourceful mid-infrared photodetectors. In this article, we present potential design considerations exploiting plasmonic effects in the conventional heterojunction mid-infrared detectors, optimized for their operation in 8–14 μm spectral range. Design issues concerning GaAs-AlGaAs based plasmonic photodetectors are investigated using modal expansion method (MEM) in conjunction with Rayleigh expansion. Simple but insightful fitting expressions useful for designing practical photodetectors are presented. The effects of crucial design parameters on the photodetector performance are discussed in detail. Using metallic grating based plasmonic element, about 20 fold absorption enhancement is predicted, which is comparable or greater than that recently reported for InAs (Quantum Dots) and GaInNAs (Quantum Well) detectors. Photodetector designs showing considerable improvement in the responsivity and the specific detectivity, compared to their nonplasmonic but otherwise identical counterpart are presented. © *2011 American Institute of Physics*. [doi:10.1063/1.3548896]

I. INTRODUCTION

Surface Plasmon (SP) based photodetectors operating in the mid-infrared spectral region ($\lambda \sim 8$–14 μm) have recently attracted much interest; see, e.g., Refs. 1–5 and the references cited therein. The interest is primarily motivated perhaps due to their applications in diverse areas such as night vision, missile tracking, medical diagnostics, environmental monitoring, and astronomy research, just to name only few. Free carrier absorption based HEterojunction Interfacial Workfunction Internal Photoemission (HEIWIP) photodetectors have shown admirable performance in the mid-infrared region.[6] These photodetectors operating up to about $\lambda = 18$ μm and showing peak responsivity about $\lambda = 10$ μm suffer from extremely low photo response and the stringent cooling requirement. Overall performance of these photodetectors is primarily limited due to extremely low optical absorption ($\sim 1\%$) in the active region (emitter), which is an inherent characteristic of free carrier mechanism. In order to make these photodetectors more efficient and cost effective for their mid-infrared operation, the issue of low optical absorption needs to be addressed. Present article address this issue and establish that the performance of heterojunction based mid-infrared detectors (e.g., HEIWIPs) can be improved significantly by utilizing the concept of metallic corrugation mediated surface plasmon enhanced absorption. Metallic corrugation in the form of periodic grating (it is to be mentioned that the periodic metallic grating exhibit superior enhancement than the nonperiodic grating[7]) plays the dual role of top metal contact as well as the light concentrator through plasmonic coupling of the exciting infrared radiation and the collective electronic oscillations at the interface of mediums with opposite permit-

tivity, e.g., metal and dielectric. Optical enhancement is facilitated by the surface wave induced optical field confined near interface. This field is characterized by its maximum at the interface and an exponential decay with the distance from it. Presence of the plasmonic element actually under suitable conditions modify the local electromagnetic environment and strengthen the light-matter interaction, which results in the enhancement of optical processes such as optical absorption. Surface plasmon enhanced optical activity is of immense interest due to its role in improving the performance of optoelectronic devices e.g., photodetectors, solar cells, LEDs, and semiconductor lasers. Since surface plasmon induced electric field decays exponentially with the distance from the interface, these are characterized by low field penetration depth. The implementation of plasmonic enhancement scheme in a real device therefore requires the placement of device active region within the penetration depth. This ensures a reasonable spatial overlap between the surface field and the active region, which is required for efficient light-matter interaction. This situation is ideally suited for heterojunction based photodetector where active region can be positioned immediately next to the plasmonic element. We would like to mention that the active region in conventional Quantum Well/Quantum Dot (QW/QD) designs is placed at a substantial distance from the top surface where plasmonic element can normally be placed. The feasibility of the proposed scheme for optical field enhancement in heterojunction based photodetectors is discussed elsewhere in this manuscript. The working mechanism in the plasmonic version remains similar to the conventional heterojunction photodetector except that the interaction occurs within a sub wavelength scale here. Since direct light-SP interaction is not feasible due to their dispersion properties, metallic corrugation Bragg scatter the incident light wave and produce series of component waves traveling in the different directions corresponding to different diffraction

---

[a] Author to whom correspondence should be addressed. Electronic mail:
uperera@gsu.edu.

orders. In-plane momentum of the component waves differ from that of the incident wave by integral multiples of magnitude of the corrugation vector $|\vec{G}| = 2n\pi/\Lambda$, where $n = 0$, ± 1, $\pm 2\ldots$, and Λ is the period of metallic corrugation. Corrugation induced momentum modulation removes inherent momentum difference of Photon-SP pair and thus increase the effective area of light collection compared to the groove size of the corrugation. By careful adjustment of the design parameters, metallic corrugation derived absorption peaks can be matched with the responsivity peaks of bare (nonplasmonic) photodetector. This is to be emphasized that the integration of metallic corrugation enhance device responsivity without causing any adverse impact on the photodetector speed.[8] Therefore, all advantages of conventional designs remain present in the plasmonic version also. Additionally, the integration of plasmonic element with HEIWIP structures operating in the mid-infrared region is particularly favorable as the required feature sizes ($\sim \mu m$) can be obtained using photolithography rather than comparatively expensive e-beam lithography, that must be used for the visible region. Metallic corrugation patterned as a periodic grating used for this purpose have been investigated for SP mediated resonant absorption in the visible region for a multilayered plasmonic structure,[9] grating optimization for the efficient SP excitation at 633 nm[10] and 476 nm,[11] and for designing improved HgCdTe[3] and angled incidence quantum-well infrared photodetectors.[12] However, the efforts are mostly concentrated on a specific wavelength or a specific detection mechanism. The optimization and design considerations suggested for visible wavelength range may not be valid for infrared region, primarily due to the significant difference in the dielectric constant of commonly used noble metals in the visible and the infrared regions. For example, Drude model based dielectric constant of gold at $\lambda = 633$ nm is $-0.296 + 0.040\ i$, whereas the dielectric constant is $-75.31 + 18.84\ i$ and $-259.38 + 128.59\ i$ at $\lambda = 5$ and $10\ \mu m$, respectively. Therefore, the design considerations suggested for visible region are not directly relevant for designing heterojunction based plasmonic detector operating in the mid-infrared region. The present article provides: (I) Design considerations to capitalize on the metallic corrugation mediated field enhancement for improving the performance of conventional heterojunction (HEIWIP) photodetector in the mid-infrared (8–14 μm) region, (II) Expressions for absorption/response peak tuning and its dependence on the geometry of plasmonic element, which are useful tool for crude estimation of the design parameters for customized photodetector structure, (III) Estimation of the improvement in the photodetector figures of merit for the experimentally feasible set of parameters.

The manuscript is organized as follows. Section II present the details of the theoretical formulation and the structure analyzed in this work. Section III present results and discussion. Conclusions are finally outlined in Sec. IV.

II. THEORETICAL MODEL

Schematic of the representative structure and the system of coordinate adopted for this work is shown in Fig. 1. This structure mimics a conventional heterojunction photodetec-

tor (see, e.g., Ref. 6) except the presence of a periodic metallic grating. The multimedia structure consists of vacuum at the top, followed by the metallic grating (plasmonic element), p-doped GaAs (emitter or active region), undoped $Al_xGa_{1-x}As$ (barrier), and undoped GaAs (substrate). For brevity, each constituent medium will be referred as MED-j (j = 0,1,2,3,4), the index-j labeling the corresponding medium number counted from the top (j = 0 → vacuum). Each constituent medium is characterized by its dielectric function (ϵ_j) and thickness (h_j). MED-j (j ≠ 1) are considered to be homogeneous along x-direction and MED-j (j = 1) which constitute the plasmonic element is inhomogeneous and consists of alternating metallic ridges and dielectric grooves of widths a_m and a_g, respectively. Each system interface is defined by its vertical position ($z = z_i$, i: 0, 1, 2, 3, e.g., i = 0 → vacuum-grating interface). The dielectric function in the plasmonic medium (j = 1) is described as:

$$\epsilon_1(x, \omega) = \epsilon_m(\omega)F(x) + \epsilon_g[1 - F(x)]. \tag{1a}$$

Here F(x) is the characteristic step function whose value is 1 when x belongs to the metal (ridge) and 0 when x belongs to the dielectric (groove) and $\epsilon_m(\epsilon_g)$ is the dielectric function of the metal (groove) region. Frequency/wavelength dependent dielectric function of the metal is calculated using Drude-Lorentz model based complex dielectric function defined as:

$$\epsilon_m(\omega) = 1 - \frac{\omega_p^2}{\omega[\omega + (\mathbf{i}/\tau)]}. \tag{1b}$$

Here ω is excitation frequency, ω_p is plasma frequency, and τ is relaxation time of metal electrons. Present analysis includes both the real {$\mathbf{Re}[\epsilon_m(\omega)]$} and the imaginary {$\mathbf{Im}[\epsilon_m(\omega)]$} parts of the complex dielectric function. Gold (Au), which is one of the most widely used plasmonic metal in practical devices, preferably due to its chemical stability
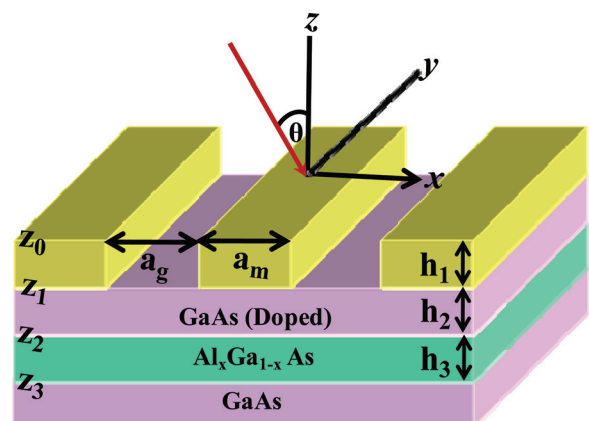

FIG. 1. (Color online) The schematic of a typical heterojunction structure considered for the analysis in this work. This mimics a typical HEIWIP structure without plasmonic element. The structure consisting of vacuum followed by the metallic corrugation, GaAs (doped), $Al_xGa_{1-x}As$ and the GaAs (undoped) substrate constitutes a multimedia system. The interface positions are labeled as z_i, where i (= 0,1,2&3) denotes the corresponding interface and h_j (j = 1, 2 and 3) denotes the thickness of the propagation layers, a_m and a_g denote widths of the metallic and grooved part of the corrugation, θ is the angle of incidence, which is measured with respect to the z-direction. For the definiteness, the metal is considered to be gold.

in the ambient conditions is the plasmonic metal considered throughout this work. The values of Drude parameters ω_p and τ for gold are 3.39×10^{15} s^{-1} and 1.075×10^{-14} s, respectively.[13] Although dielectric in the groove is considered as vacuum here ($\epsilon_g = 1$), the analysis applies to any arbitrary dielectric and can be easily incorporated in the present formulation.

The dielectric function of doped-GaAs is modeled using Drude model for free carriers and the multioscillator model for optical phonons in accordance with Ref. 14 as:

$$\epsilon(\omega) = \epsilon_\infty \left\{ 1 - \frac{\omega_P^2}{\omega[\omega + (i/\tau)]} \right\} + \frac{\omega_{TO}^2(\epsilon_S - \epsilon_\infty)}{\omega_{TO}^2 - \omega^2 - i\omega\gamma}. \quad (1c)$$

In Eq. (1c), ϵ_∞ and ϵ_S are the high frequency and the static dielectric constants of the intrinsic semiconductor, ω_p and τ are the plasma frequency and carrier lifetime, ω_{TO} and γ are the transverse optical phonon frequency and phonon damping coefficient. The doping rates are included in the model by considering the effect of doping concentration on carrier plasma frequency (ω_p) through relation, $\omega_p = \sqrt{(N_p q^2 / \epsilon_v \epsilon_s m^*)}$, where m^* and N_p are the carrier effective mass and doping dependent free carrier concentration, ϵ_v and ϵ_s are vacuum permittivity and static dielectric constant, and q is the elementary charge. The values of the parameters used for these calculations are:[14,15] $\epsilon_\infty = 10.89$, $\epsilon_s = 12.90$, $\tau = 1.2 \times 10^{-14}$ s, $\hbar\omega_{TO} = 33.25$ meV, $\hbar\gamma = 0.25$ meV, $m^* = 0.50\ m_0$. Whole multimedia system is treated to be isotropic and homogeneous along y-direction.

The structure is excited from vacuum side (dielectric constant ϵ_0) by the plane wave of wavelength λ and wave vector $\vec{k}_0(|\vec{k}_0| = 2\pi/\lambda)$ at an angle of incidence θ measured relative to $+z$-axis. Since nonzero electric field in the direction normal to the interface is required for plasmonic excitation, this being zero for transverse electric (TE) wave, the excitation electromagnetic wave is considered to be transverse magnetic (TM) described as:

$$\mathbf{E}(x, z, \omega) = (\mathbf{E}_x, 0, \mathbf{E}_z)\exp[-i(\sqrt{\epsilon_0}\,k_x x + \sqrt{\epsilon_0}\,k_z z + \omega t)], \quad (2a)$$

$$\mathbf{H}(x, z, \omega) = (0, \mathbf{H}_y, 0)\exp[-i(\sqrt{\epsilon_0}\,k_x x + \sqrt{\epsilon_0}\,k_z z + \omega t)]. \quad (2b)$$

The nonzero field components $\mathbf{E}_x$, $\mathbf{H}_y$, $\mathbf{E}_z$ in Eqs. (2a and 2b) are not independent and are coupled through Maxwell's equations as follows:

$$\mathbf{E}_x(x, z, \omega) = -\frac{i}{\omega\epsilon_v\epsilon} \frac{\partial \mathbf{H}_y(x, z, \omega)}{\partial z},$$
$$\mathbf{E}_z(x, z, \omega) = \frac{i}{\omega\epsilon_v\epsilon} \frac{\partial \mathbf{H}_y(x, z, \omega)}{\partial x}. \quad (2c)$$

Here ϵ_v and ϵ stands for vacuum permittivity and the dielectric constant (or relative permittivity) of the corresponding medium. Additionally, $\mathbf{H}_y$ satisfy the following

wave equations in the grating (Eq. 2d) and the homogeneous (Eq. 2e) mediums, respectively,

$$\left[\frac{\partial^2}{\partial x^2} + \frac{\partial^2}{\partial z^2} + k_0^2\,\epsilon(x, \omega) \right] H_y(x, z, \omega) = 0, \quad (2d)$$

$$\left[\frac{\partial^2}{\partial z^2} + k_{zn}^2\,\epsilon(\omega) \right] H_y(x, z, \omega) = 0. \quad (2e)$$

Here H_y and $\mathbf{H}_y$ are related as $H_y = \sqrt{(\mu_v/\epsilon_v)}\,\mathbf{H}_y$, μ_v and ϵ_v stand for vacuum permeability and permittivity, respectively, and k_{zn} in the respective medium j is defined by $k_{zn}^{(j)} = \sqrt{\epsilon_j k_0^2 - k_{xn}^2}$ with $k_{xn} = k_0 \sin\theta + |\vec{G}|$. Remaining symbols in Eqs. (2a–2e) have their standard physical definitions. Evidently, once H_y is known from the solution of Eqs. (2d and 2e), other nonzero field components ($\mathbf{E}_x$, $\mathbf{E}_z$) can be calculated from Eq. (2c). Electromagnetic field in the inhomogeneous plasmonic element/metal grating is computed following the approach originally developed by Sheng et al.[16] within the physical constraints of the field continuity conditions and Bloch-Floquet theorem. This method known as modal expansion method (MEM) first requires solving the grating dispersion equation to find out the eigenvalues of the electromagnetic eigenmodes in the grating region. The eigenmodes must satisfy the boundary conditions at the lateral interfaces (metal/vacuum) along y-z plane. This means the continuity of H_y and $[(\partial H_y/\partial x)/\epsilon]$, which ensures the continuity of the tangential components of the magnetic field (H_y) and the electric field (E_z) respectively. In MEM, the electromagnetic field in the grating region (MED-1) is expressed as the basis set of eigenmodes of an infinite periodic structure, obtained from the periodicity condition. Using MEM, the field $H_y^{(1)}(x, z, \omega)$ can be written as:[17]

$$H_y^{(1)}(x, z, \omega) = \sum_l \xi_l(x)[A_l^{(1)}\exp(-ik_{zl}^{(1)}z) + B_l^{(1)}\exp(ik_{zl}^{(1)}z)]. \quad (3a)$$

Here $k_{zl}^{(1)}$ defines grating eigenmodes characterized by the index $l = 0, 1, 2, \ldots \infty$, labeling the eigenmodes in their increasing order. These eigenmodes appear as the infinite complex solutions of the following nonlinear dispersion relation:[17]

$$\frac{\Omega_l^2 + 1}{2\Omega_l}\sin(\beta_{ml}a_{ml})\sin(\beta_{gl}a_{gl}) - \cos(\beta_{ml}a_{ml})\cos(\beta_{gl}a_{gl})$$
$$+ \cos\left(\frac{2\pi\Lambda}{\lambda}\sin\theta \right) = 0, \quad (3b)$$

where

$$\Omega_l = \frac{\epsilon_m \beta_{gl}}{\epsilon_g \beta_{ml}}, \quad \beta_{ml} = \sqrt{\epsilon_m k_0^2 - (k_{zl})^2},$$
$$\beta_{gl} = \sqrt{\epsilon_g k_0^2 - (k_{zl})^2}, \quad \Lambda = a_m + a_g, \quad (3c)$$

$$\xi_l(x) = \begin{cases} D_{ml}\exp[i\beta_{ml}(x - \Lambda)] + F_{ml}\exp[-i\beta_{ml}(x - \Lambda)], & \text{for } 0 < x < a_m \\ D_{gl}\exp[i\beta_{gl}(x - \Lambda - a_m)] + F_{gl}\exp[-i\beta_{gl}(x - \Lambda - a_m)], & \text{for } a_m < x < \Lambda, \end{cases} \quad (3d)$$

with

$$D_{ml} = 1, \tag{3e}$$

$$F_{ml} = \frac{1 + \Omega_l}{1 - \Omega_l} \frac{\exp(i\beta_{ml}a_m) - \exp[i(k_x\Lambda - \beta_{gl}a_g)]}{\exp(-i\beta_{ml}a_m) - \exp[i(k_x\Lambda - \beta_{gl}a_g)]}, \tag{3f}$$

$$D_{gl} = \frac{(1 + \Omega_l)\exp(i\beta_{ml}a_m) + (\Omega_l - 1)\exp(-i\beta_{ml}a_m)F_{ml}}{2\Omega_l}, \tag{3g}$$

$$F_{gl} = \frac{(\Omega_l - 1)\exp(i\beta_{ml}a_m) + (\Omega_l + 1)\exp(-i\beta_{ml}a_m)F_{ml}}{2\Omega_l}. \tag{3h}$$

In order to calculate k_{zl}, Eq. (3b) is solved numerically. Noticeably, the solution of Eq. (3b) is the most sensitive part of these calculations. It is essential to ensure that no modes are missing in the computation as this will lead to the nonconvergence in the computation. In the present analysis, solutions with precision $\sim 1 \times 10^{-14}$ were obtained and the modal density was in accordance with Ref. 18. Once grating eigenmodes k_{zl} are known, the electromagnetic field in all the mediums can be written as the general solution of Maxwell's equations. The equations governing the electromagnetic field distribution in different mediums of the considered system are:

$$H_y^{(0)}(x, z, \omega) = A^{(0)}\exp[i(k_x x - k_z^{(0)}z)] + \sum_n B_n^{(0)}\exp[i(k_{xn}x + k_{zn}^{(0)}z)], \tag{4a}$$

$$H_y^{(1)}(x, z, \omega) = \sum_l \xi_l(x)[A_l^{(1)}\exp(-ik_{zl}^{(1)}z) + B_l^{(1)}\exp(ik_{zl}^{(1)}z)], \tag{4b}$$

$$H_y^{(2)}(x, z, \omega) = \sum_n A_n^{(2)}\exp\{i[k_{xn}x - k_{zn}^{(2)}(z - z_1)]\} + \sum_n B_n^{(2)}\exp\{i[k_{xn}x + k_{zn}^{(2)}(z - z_1)]\}, \tag{4c}$$

$$H_y^{(3)}(x, z, \omega) = \sum_n A_n^{(3)}\exp\{i[k_{xn}x - k_{zn}^{(3)}(z - z_2)]\} + \sum_n B_n^{(3)}\exp\{i[k_{xn}x + k_{zn}^{(3)}(z - z_2)]\}, \tag{4d}$$

$$H_y^{(4)}(x, z, \omega) = \sum_n A_n^{(4)}\exp\{i[k_{xn}x - k_{zn}^{(4)}(z - z_3)]\}. \tag{4e}$$

The coefficients A's and B's in Eqs. (4a)–(4e) are the amplitudes of forward and reverse propagating waves, respectively. Summation in these equations extend from $-\infty$ to $+\infty$. Superscript on these coefficients denotes corresponding medium number (j) and the subscript denotes order $n = 0, \pm 1, \pm 2 \ldots$ of the diffracted wave. Additionally, the boundary condition that no reverse propagating wave exists in the last medium (j = 4) is implemented. This makes the reflection amplitude coefficient zero in that medium. The set of Eqs. (4a)–(4e) provides field distribution in the individual medium. The field distribution must obey the conditions of continuity of the tangential field components H_y and E_x at the interfaces, which corresponds to the continuity of H_y and $(\partial H_y/\partial z)/\epsilon$. These boundary conditions produce a set of two

algebraic equations at each interface. For example, the field continuity at $z = z_0$ (which correspond to the vacuum-grating interface) produce:

$$B_n^{(0)} - \sum_l \Gamma_{ln}^{(1)}A_l^{(1)} - \sum_l \Gamma_{ln}^{(1)}\exp[ik_{zl}^{(1)}h_1]\widehat{B}_l^{(1)} = -A^{(0)}\delta_{n0}, \tag{5a}$$

$$(-k_{z0}^{(0)}/\epsilon_0)B_n^{(0)} - \sum_l k_{zl}^{(1)}\Gamma_{ln}^{(2)}A_l^{(1)}$$
$$+ \sum_l k_{zl}^{(1)}\Gamma_{ln}^{(2)}\exp(ik_{zl}^{(1)}h_1)\widehat{B}_l^{(1)} = -k_{z0}^{(0)}A^{(0)}\delta_{n0}. \tag{5b}$$

Field continuity at the lower grating-homogeneous layer interface at $z = z_1$ produce:

$$\sum_l \Gamma_{ln}^{(1)}\exp(ik_{zl}^{(1)}h_1)A_l^{(1)}$$
$$+ \sum_l \Gamma_{ln}^{(1)}\widehat{B}_l^{(1)} - A_n^{(2)} - \exp(k_{zl}^{(2)}h_2)\widehat{B}_n^{(2)} = 0, \tag{5c}$$

$$\sum_l k_{zl}^{(1)}\Gamma_{ln}^{(2)}\exp(ik_{zl}^{(1)}h_1)A_l^{(1)} - \sum_l k_{zl}^{(1)}\Gamma_{ln}^{(2)}\widehat{B}_l^{(1)}$$
$$- (k_{zn}^{(2)}/\epsilon_2)A_n^{(2)} + (k_{zn}^{(2)}/\epsilon_2)\exp(ik_{zn}^{(2)}h_2)\widehat{B}_n^{(2)} = 0. \tag{5d}$$

Field continuity at the interface $z = z_2$ produce:

$$A_n^{(2)}\exp(ik_{zn}^{(2)}h_2) + \widehat{B}_n^{(2)} - A_n^{(3)} - \widehat{B}_n^{(3)}\exp(ik_{zn}^{(3)}h_3) = 0, \tag{5e}$$

$$(k_{zn}^{(2)}/\epsilon_2)[A_n^{(2)}\exp(ik_{zn}^{(2)}h_2)] - (k_{zn}^{(2)}/\epsilon_2)\widehat{B}_n^{(2)}$$
$$- (k_{zn}^{(3)}/\epsilon_3)[A_n^{(3)} - \widehat{B}_n^{(3)}\exp(ik_{zn}^{(3)}h_3)] = 0. \tag{5f}$$

Field continuity at the last interface $z = z_3$ produce:

$$A_n^{(3)}\exp(ik_{zn}^{(3)}h_3) + \widehat{B}_n^{(3)} - A_n^{(4)} = 0, \tag{5g}$$

$$(k_{zn}^{(3)}/\epsilon_3)[A_n^{(3)}\exp(ik_{zn}^{(3)}h_3) - \widehat{B}_n^{(3)}] - (k_{zn}^{(4)}/\epsilon_4)A_n^{(4)} = 0. \tag{5h}$$

In Eqs. [(5a)–(5d)], Γ is defined as:

$$\Gamma_{ln}^{(1)} = \frac{1}{\Lambda}\int_0^\Lambda \xi_l(x)\exp(-ik_{xn}x)dx, \tag{5i}$$

$$\Gamma_{ln}^{(2)} = \frac{1}{\Lambda}\int_0^{a_m} \frac{\xi_l(x)}{\epsilon_m(x)}\exp(-ik_{xn}x)dx$$
$$+ \frac{1}{\Lambda}\int_{a_m}^\Lambda \frac{\xi_l(x)}{\epsilon_g(x)}\exp(-ik_{xn}x)dx. \tag{5j}$$

For improved computational efficiency, the following transformation is used:

$$B_n^{(j)} = \widehat{B}_n^{(j)}\exp(ik_{zn}^{(j)}h_j), \text{ for } j = 1, 2 \& 3. \tag{5k}$$

The system of Eqs. (5a)–(5d) exhibit unique solutions for amplitude coefficients A's and B's. This system of linear algebraic equations is solved numerically using built-in functions available in Matlab 7.5.0 (R2007b). It is to be

emphasized that, as the summation extends from $-\infty$ to $+\infty$, an exact field treatment of the problem corresponds to the solution of an infinite number of algebraic equations. Therefore, practically, the number of equations (say N) needs to be truncated and this limit is determined by ensuring the convergence of reflection (R), transmission (T), and absorption (A) defined as:

$$T = \frac{k_{zn}^{(3)}}{\epsilon_3 k_{zn}^{(0)}} \left| \frac{A_0^{(3)}}{A^{(0)}} \right|^2, \quad R = \frac{k_{zn}^{(0)}}{\epsilon_0 k_{z0}^{(0)}} \left| \frac{B_0^{(0)}}{A^{(0)}} \right|^2, \quad \text{and}$$

$$A = 1 - (T + R).$$

(6)

For present calculations, truncation beyond $n \sim 20$ (N = 2n + 1 = 41) normally does not involve any truncation error and, therefore, $n > 20$ is used throughout the analysis. Computationally, there exists a wide length scale where period $\sim$ wavelength and the grating height $\sim$10s of nanometers. The approach used here is versatile as it can be used for the variety of photodetectors and can be easily extended to the different wavelength ranges and also to the different material systems. The responsivity is calculated using, $R = \eta q\lambda/hc$ where h is Planck's constant, η is the total quantum efficiency. The total quantum efficiency (η) is calculated as the product of absorption efficiency (η_a) and internal photoemission efficiency (η_i) assuming full collection efficiency which is generally the case for these devices. The absorption efficiency (η_a) is calculated using, $\eta_a = 2k_0 h_2 \text{Im}[\epsilon_2(\omega)] |\bar{E}|^2/E_0^2$, where E is the electric field of the electromagnetic wave in the emitter region, E_0 is the electric field of the incident plane wave, h_2 is the thickness of the emitter. The internal photoemission efficiency (η_a) is calculated using the model described in Refs.[19] and [20].

III. RESULTS AND DISCUSSION

In this section, results of our investigations concerning design considerations for heterojunction based plasmonic photodetector structure shown in Fig. 1 are presented. The structure mimics a conventional HEIWIP detector without metallic grating.[6] Unless mentioned otherwise, following parameters have been used for present analysis: angle of incidence $\theta = 0°$, fill factor f(= a_m/Λ) = 0.5, h_2 = 100 nm, h_3 = 120 nm, emitter doping = 1×10^{19} cm^{-3}. The values of basic semiconductor parameters for GaAs/Al$_x$Ga$_{1-x}$As are used from Ref. [15]. These parameters are typical of the practical devices and are completely accessible from experimental point of view. As mentioned in Sec. I, penetration depth of the field is a decisive parameter for designing an active plasmonic device. For plasmonic approach to be feasible, device active region must be placed within the penetration distance measured from plasmonic element. For the structure under consideration this can be visualized from Fig. 2 where variation of the z-component of the electric field intensity $|E_z|^2$ as a function of the distance from metal-emitter interface is plotted for various metallic heights ($h_1 = 30, 40, 50, 60, 80, 100,$ and 150 nm) and period (Λ) 2.8 μm of the corrugation for excitation radiation of wavelength (λ) = 10 μm. The filed decay exponentially with the distance from the
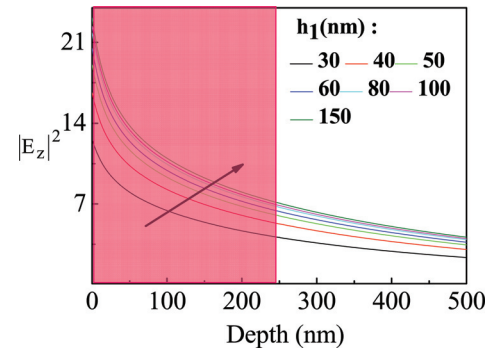

FIG. 2. (Color online) The variation of the electric field intensity $|E_z|^2$ of the z-component of the electric field E_z as a function of the distance from the metal/emitter interface for the excitation of a plane wave of wavelength $\lambda = 10$ μm for different metal heights (h_1) and the grating with period (Λ) = 2.8 μm. Noticeably, the strong field exists up to $\sim$300 nm (shown by shaded region). This shows the practicability of the proposed approach for these structures.

metal-emitter interface as is anticipated for surface confined waves. For the structure under consideration, the penetration depth defined as the distance for e^{-1} decay is about 250 nm on the average. The shaded part indicates the region of existence of strong surface field. Interestingly, magnitude of the field and its penetration increases with the metallic height (h_1) up to about 100 nm, where both becomes independent of any further increase in h_1. This situation is ideally suited for heterostructure based photodetector where typical effective active region thickness after etching is approximately 100 nm and plasmonic element can be placed just above this.

Next we calculate absorption spectra for the structure shown in Fig. 1 with metal dimensions appropriate for mid-infrared region. Spectra for three different grating periods ($\Lambda = 2.8, 3.2$ & 3.6 μm) are shown in Figs. 3, 4, and 5, respectively. For each case, the dependence of spectrum on metallic height (h_1) is also included. For sake of comparison, absorption spectra for bare structure (nonplasmonic) are also shown. The main features of these spectra are: (i) Appearance of resonant absorption peaks spanning mid-infrared spectral window, (ii) Blue-shift of resonant wavelength λ_p with increasing metallic height h_1 till λ_p becomes independent of further increase at a
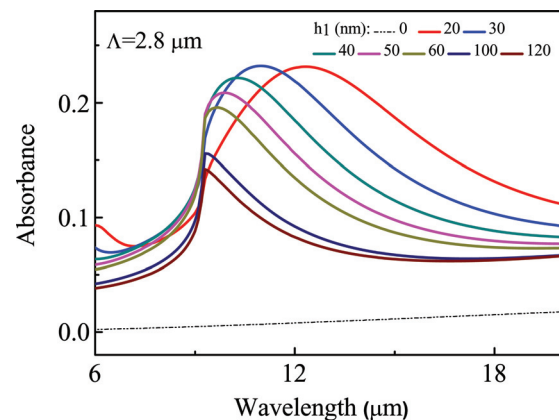

FIG. 3. (Color online) The calculated absorption spectrum for the structure shown in Fig. 1 for $\Lambda = 2.8$ μm and for different grating heights. The absorption for the structure without grating is also shown here (dotted curve). It can be seen that the absorption peak can be fine tuned by varying the grating height. Larger the thickness, shorter is the absorption peak wavelength.
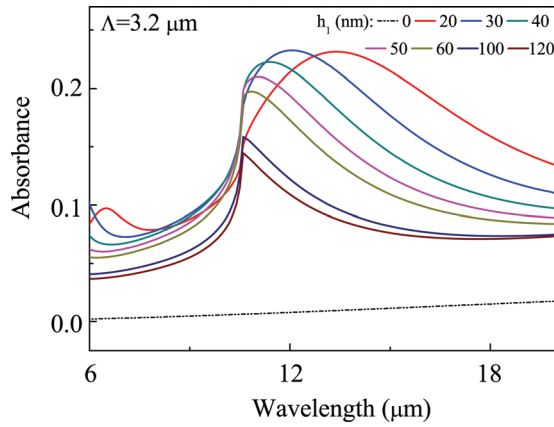
FIG. 4. (Color online) The calculated absorption spectrum for the structure shown in Fig. 1 with $\Lambda = 3.2~\mu$m and for different grating heights. The absorption for the structure without grating is also shown here (dotted curve). The absorption peak can be fine tuned by varying the metal height. Larger the thickness, shorter is the absorption peak wavelength.

FIG. 6. Calculated absorption peak wavelength λ_p dependence on the grating height (h_1) as a function of different grating periods, $\Lambda = 2.8$, 3.2, and 3.6 μm. The corresponding exponential fittings are also shown (scattered points) for each case. The blue-shift and the saturation of the peak wavelength λ_p are explained in terms of the Rayleigh anomaly. We note that the resonance blue shifts as the grating height is increased and then becomes independent of further increase of grating height h_1.

characteristic wavelength, (iii) Red-shift of resonant wavelength λ_p with increasing grating period Λ, (iv) Substantial absorption enhancement in the presence of plasmonic element relative to the bare structure, (v) Increased peak asymmetry toward shorter wavelengths. It is to be mentioned that although results are shown only for the normal incident wave ($\theta = 0°$), absorption peak position remain almost unaffected with increase in θ as $k_0 \sin\theta$ still remains significantly smaller relative to the primitive grating vector magnitude ($2\pi/\Lambda$).

Resonant absorption originated from plasmonic interaction can be utilized for improving the figures of merit of proposed photodetector. The observed effects of metallic height h_1 including blue-shift in Figs. 3, 4, and 5 can be best explained by analyzing the variation of resonant wavelength λ_p with metallic height. As shown in Fig. 6, this peak wavelength variation can be fitted into a mathematical expression of the form:

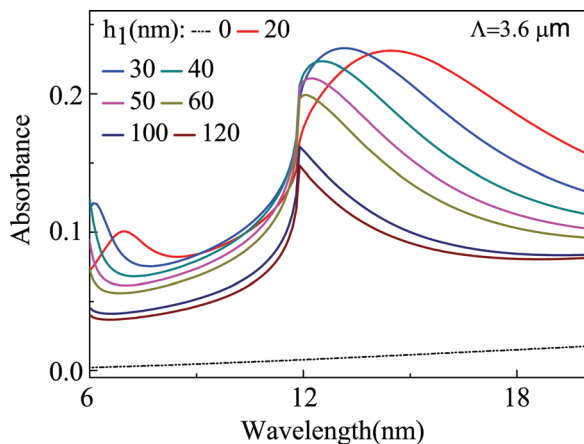$$\lambda_p = \lambda_0 \exp[-(h_1/H)] + \lambda_s. \tag{7}$$

Here λ_0, λ_s and H are fitting parameters and can be assigned physical meanings. We attribute λ_0 the role of maximum peak wavelength, H the role of saturation peak wavelength, and λ_s the role of characteristic metallic height for blueshift. The list of fitting parameters for three different grating periods ($\Lambda = 2.8$, 3.2, and 3.6 μm) is presented in Table I. Evidently, λ_0 and λ_s increase with the grating period while H decrease with the grating period. This means that the longer the grating period, the higher the rate of blue-shift with metallic height. We would like to mention that the saturation of peak wavelength beyond a particular grating height was recently also reported by Gadson et al.[21] in the visible region ($\lambda = 400 - 800$ nm). We attribute the saturation of the peak wavelength to the appearance of Rayleigh anomaly. Rayleigh anomaly corresponds to the rapid variation in the amplitudes of diffraction orders due to the onset (evanescent-propagating) or disappearance (propagating-evanescent) of higher order modes. This occurs at a characteristic wavelength called Rayleigh wavelength λ_R. For wavelengths shorter than λ_R, higher order modes becomes propagating. For wavelengths above λ_R, higher order modes becomes evanescent, which does not contribute to the absorption. To show this more convincingly, calculated absorption spectra considering zeroth and all modes are shown in Figs. 7 and 8

FIG. 5. (Color online) The calculated absorption spectrum for the structure shown in Fig. 1 with $\Lambda = 3.6~\mu$m, and for different grating heights. The absorption for the structure without metallic grating is also shown (dotted curve). Absorption peak can be fine tuned by varying the grating height. Larger the thickness, shorter is the absorption peak wavelength.
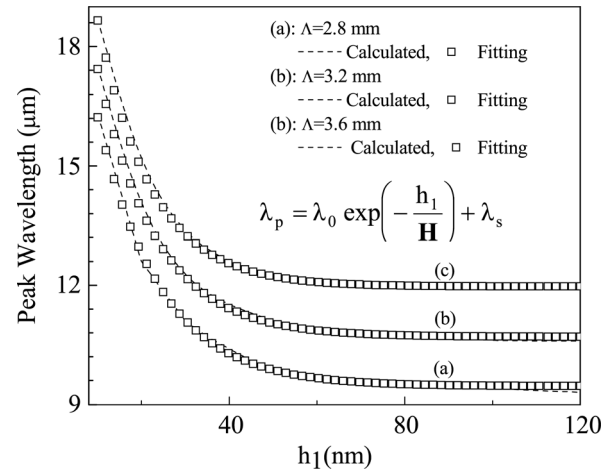
TABLE I. List of the fitting parameters of expression, $\lambda_p = \lambda_0 \exp[-(h_1/H)] + \lambda_s$ and Rayleigh wavelength λ_R calculated using analytical $\{\lambda_R^{\pm 1} = \Lambda\sqrt{\epsilon}[1 \mp (\sqrt{\epsilon_0} \sin\theta / \sqrt{\epsilon})]\}$ and computational approach (discussed in Sec. II).

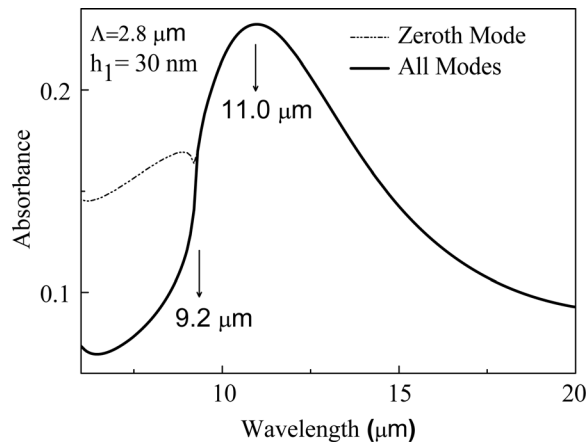| Grating Period Λ(μm)	Characteristic Height H (μm)	λ_0 (μm)	λ_S (μm)	Calculated λ_R (μm)	Analytical λ_R (μm)
2.8	14.23	13.66	9.46	9.20	9.24
3.2	13.37	14.22	10.70	10.60	10.56
3.6	12.28	15.10	11.97	11.90	11.80

FIG. 7. The calculated absorption spectra for the structure shown in Fig. 1 with grating period $\Lambda = 2.8$ μm and grating height $h_1 = 30$ nm. Results are shown for zeroth mode (dotted curve) and all radiative modes (solid curve). Arrows indicates Rayleigh wavelength (left) and the peak wavelength (right). Absorption changes suddenly at Rayleigh wavelength (9.2 μm) due to the redistribution of energy into different modes. Below Rayleigh wavelength, onset of higher order radiative modes occurs.
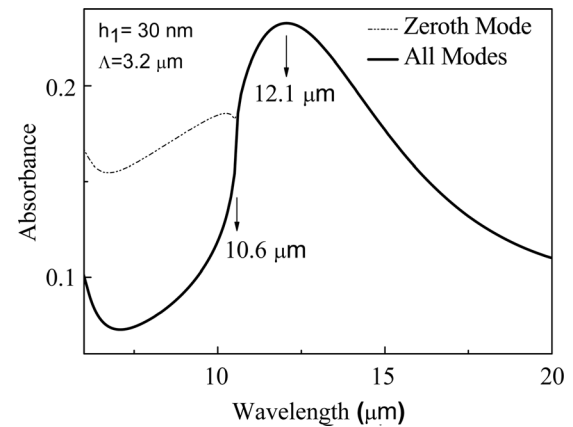

FIG. 8. The calculated absorption spectra for the structure shown in Fig. 1 with grating period $\Lambda = 3.2$ μm and grating height $h_1 = 30$ nm. Results are shown for zeroth mode (dotted curve) and all radiative modes (solid curve). Arrows indicates Rayleigh wavelength (left) and the peak wavelength. Absorption changes suddenly at Rayleigh wavelength (10.6 μm) due to the redistribution of the energy into different modes. Below Rayleigh wavelength, onset of higher order radiative modes occurs.

for two different grating periods ($\Lambda = 2.8$ and 3.2 μm) and fixed metallic height ($h_1 = 30$ nm). Evidently, the wavelength where zeroth order efficiency starts differing from that due to all order efficiencies can be noticed clearly at $\lambda = 9.2$ and 10.6 μm for $\Lambda = 2.8$ μm, respectively. Surprisingly, these wavelengths are very close to the above calculated saturation wavelength λ_s for these cases. As a further confirmation to the fact, Rayleigh wavelengths are also calculated using analytical expression:[17]

$$\lambda_R^{\pm 1} = \Lambda \sqrt{\epsilon}[1 \mp (\sqrt{\epsilon_0} \sin\theta / \sqrt{\epsilon})]. \qquad (8)$$

Analytically, calculated data are included in Table I. In Eq. (8), ± 1 represent the diffraction order, Λ is the grating period, ϵ_0 is the dielectric constant of the incident medium ($j = 0$), ϵ is the dielectric constant of the last medium ($j = 4$). For normal incidence ($\theta = 0°$), $+$1st and $-$1st order Rayleigh wavelength will be same. Rayleigh wavelength for higher order modes will appear outside the range of our present interest. Rayleigh wavelength for $\Lambda = 3.2$ μm grating is 10.6 μm, which is also as expected analytically. It can be seen that Rayleigh wavelength remains unaffected by the variation in metallic grating height. Noticeably, the sharp fall in the vicinity of a particular wavelength on the left side of resonant peak is present for all grating periods. Two curves differ only in the short wavelength end up to a particular wavelength beyond which two curves are identical. It can be seen from the basic grating equation that the number of modes for shorter wavelengths will be more. Diffraction angle for higher order waves gets smaller as the wavelength decrease. This can also give rise to different resonant positions and absorption values. The role of grating period Λ in resonant wavelength λ_p tuning is summarized in Fig. 9 for gratings of different height ($h_1 = 30$, 60 and 120 nm). The variation can be best described by a simple straight line equation of the form:

$$\lambda_p(\mu m) = u \times \Lambda(\mu m) + c. \qquad (9)$$

Here u and c denotes the slope and the intercept, respectively, u values being 2.78, 2.97, 3.21 and c values being 3.27, 1.41, 0.32 for $h_1 = 30$, 60 and 120 nm, respectively. Higher the grating height, higher the slope but lower the intercept. The peak wavelength shift is caused by the change of Brillouin zone size resulting from the change in the magnitude of the Bragg vector K ($= m\pi/\Lambda$) with changing Λ. The change in K leads to a change in the magnitude of the SP wave vector, $k_{sp} = (\epsilon/c) \sin\theta + 2$ K, and hence the change in the resonant wavelength, $\lambda_p = 2\pi/k_{sp}$. The variation of peak absorbance on the grating period and the grating height is shown in Fig. 10. It can be seen that the peak absorption is independent of the grating period but depends strongly on the grating height. The effect of emitter thickness on the resonant wavelength λ_p is shown in Fig. 11 for different grating heights. Interestingly, resonant wavelength λ_p is independent
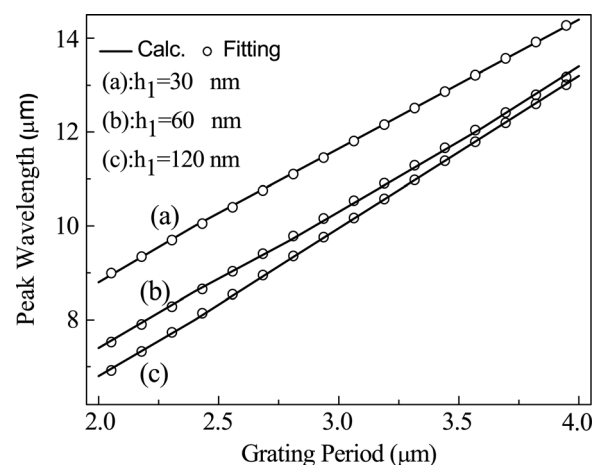

FIG. 9. The calculated absorption peak wavelength λ_p as a function of grating period Λ. Results are shown for three different grating heights (a) $h_1 = 30$ nm, (b) $h_1 = 60$ nm, and (c) $h_1 = 120$ nm. The peak wavelength λ_p has a linear dependence on the grating period Λ. The corresponding linear fittings are shown by empty circles. Such a linear variation bears significance due to its role in designing detector with desired peak wavelength.
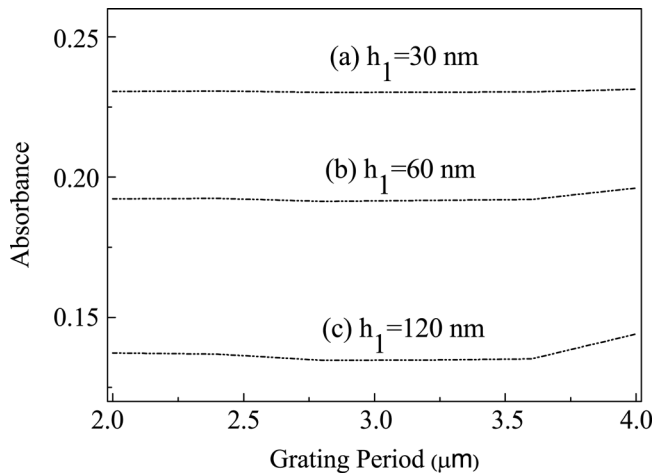
FIG. 10. The calculated peak absorption as a function of grating period Λ. Results are shown for three different heights of the grating (a) $h_1 = 30$ nm, (b) $h_1 = 60$ nm, and (c) $h_1 = 120$ nm. Maximum absorption remains almost constant with the grating period but strongly depends on the grating height.

FIG. 12. (Color online) Estimated absorption enhancement as a function of emitter thickness h_2 for proposed plasmonic detector with $\Lambda = 3.2$ μm and $h_1 = 60$ nm. Plots for three excitation wavelengths (a) $\lambda = 11$ μm, (b) $\lambda = 12$ μm, and (c) $\lambda = 10$ μm are shown. It can be seen that the enhancement is more at $\lambda = 11$ μm since this is close to the resonant wavelength for $\Lambda = 3.2$ μm and $h_1 = 60$ nm (see Fig. 4). For practical emitter thickness range absorption is significantly increased which is about 20 fold relative to the nonplasmonic counterpart.

of the emitter thickness except a moderate dependence for very small metallic heights. This is important from design point of view as emitter thickness does not affect resonant wavelength and hence can be chosen independently. The resonant wavelength can be tuned by controlling the geometry of plasmonic element. The quantitative estimation of absorption enhancement as a function of emitter thickness for three different wavelengths ($\lambda = 10$, 11, and 12 μm) is presented in Fig. 12. It can be seen that the enhancement is more at $\lambda = 11$ μm since this is close to the resonant wavelength for $\Lambda = 3.2$ μm and $h_1 = 60$ nm. (see Fig. 5). For practical emitter thickness range, absorption is significantly increased which is about 20 fold relative to the nonplasmonic device. We would like to mention that this enhancement is comparable to the recently reported absorption enhancement for InAs QD photodetectors using two-dimensional hole array (2DHA),[1] and for GaInNAs QW based MSM photodetector[22] where enhance-
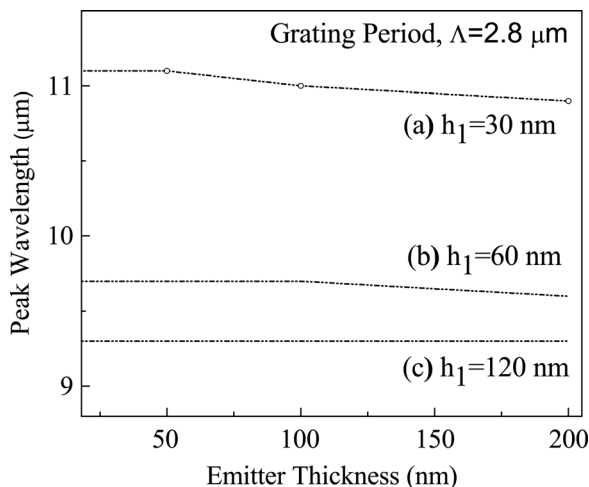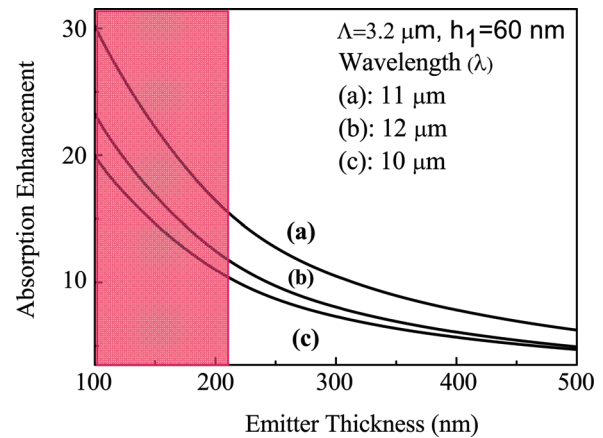
ment factor ~20 and 16 have been reported. The increased asymmetry of the absorption peak with increased grating height can be attributed to the merger of resonant peak position with Rayleigh wavelength. Sharpness of the absorption peaks can be further tuned by varying groove aspect ratio (ratio of grating height and the groove width).

The calculated responsivity (R) data for the structure shown in Fig. 1 considering grating with period (Λ) = 2.8 μm and metal heights (h_1) = 30, 60, and 120 nm are presented in Fig. 13. In these calculations, internal quantum efficiency and absorption efficiency have been estimated based on the method described in Refs. 19 and 20. Responsivity is calculated using $R = \eta q \lambda / hc$ where η is the quantum efficiency and remaining symbols have their standard physical definitions and values. For comparison purpose, the responsivity data for
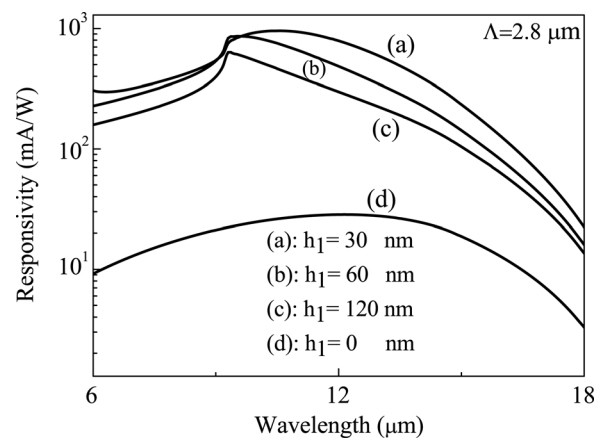

FIG. 11. The calculated peak wavelength λ_p as a function of emitter thickness h_2. The plots for $\Lambda = 2.8$ μm and grating heights, (a) $h_1 = 30$ nm, (b) $h_1 = 60$ nm and (c) $h_1 = 120$ nm are shown. Evidently, peak wavelength is independent of the emitter thickness except a moderate dependence for very small metallic height. The peak wavelength therefore can be tuned by plasmon element.

FIG. 13. The calculated responsivity (R) for the structure shown in Fig. 1 considering grating with period $\Lambda = 2.8$ μm and metal heights $h_1 = 30$, 60, and 120 nm. For comparison purpose, R without plasmonic element ($h_1 = 0$ nm) is also shown in the figure. Responsivity is calculated using $R = \eta q \lambda / hc$ where η is the quantum efficiency and remaining symbols have their standard physical definitions and values. For the chosen set of plasmonic element parameters, a significant improvement relative to the conventional designs is evident.
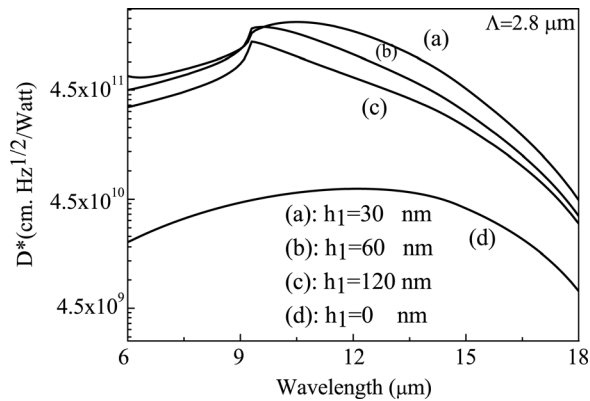
FIG. 14. The calculated specific detectivity (D*) estimated using parameters for the structure shown in Fig. 1 considering grating with period $\Lambda = 2.8$ μm and metal heights $h_1 = 30$, 60, and 120 nm. For comparison purpose, D* without plasmonic element ($h_1 = 0$ nm) is also shown in the figure. For these estimations, photosensitive area ($S = 1.6 \times 10^{-3}$ cm^2), typical for fabricated HEIWIP detector is used (Ref. 6). Similarly, a realistic noise-current density ($I_{noise} = 2 \times 10^{-14}A/\sqrt{Hz}$) value, recently reported for experimentally measured HEIWIP device at 4.2 K is assumed (Ref. 6).

the bare structure (without plasmonic element) is also included in the figure. Figure shows that the calculated peak responsivity for the bare structure is 28.39 mA/W at $\lambda = 12.1$ μm. Moreover, the responsivity values estimated for the devices with plasmonic element are: 957.94, 863.15, and 633.21 mA/W, respectively, for $h_1 = 30$, 60, and 120 nm. Higher responsivity for the devices with plasmonic element relative to the bare device is resulted from the plasmonic effects. Since the parameters used for these calculations are experimentally accessible and typical for HEIWIP structures, the theoretically predicted plasmonic enhancement should be manifested by a real photodetector device.

Finally, the effect of plasmonic element on another crucial figure of merit used to characterize photodetector performance, namely, specific detectivity (D*), which depends on the responsivity (R), the photosensitive area (S), and the noise current density (I_{noise}) of the photodetector ($D^* = $ R S/ I_{noise}) is investigated. The data for plasmonic element with period (Λ) = 2.8 μm, and metal heights (h_1) = 30, 60, and 120 nm are presented in Fig. 14, where for the sake of comparison D* without plasmonic element ($h_1 = 0$ nm) is also included. For present calculations, photosensitive area ($S = 1.6 \times 10^{-3}$ cm^2), which is typical for fabricated HEIWIP detector is used.[6] Similarly, a realistic noise-current density ($I_{noise} = 2 \times 10^{-14}A/\sqrt{Hz}$) value, recently reported for experimentally measured similar HEIWIP device at 4.2 K is assumed.[6] This can be concluded from Figs. 13 and 14 that a significant improvement in the detector figures of merit such as the responsivity and the specific detectivity are achievable by integrating a plasmonic element in the form of metallic grating.

IV. CONCLUSIONS

Using detailed numerical investigations based on modal expansion method, we have established the feasibility of metallic corrugation based plasmonic element for enhancing the performance of heterojunction based conventional mid-infrared photodetector. Through proper selection of the dimensions of plasmonic element, about 20 fold enhancement of optical absorption is predicted. The dimensions of plasmonic element are shown to have strong effect on the detector figures of merit, e.g., optical absorption, responsivity, and detectivity. Simple expressions for designing customized photodetector have been presented, which can act as the crude expressions for designing photodetector without performing complicated computation. Theoretically calculated results are shown to provide about an order enhancement of responsivity and detectivity with optimized parameters. Present investigations in the backdrop of the facts that required plasmonic element for heterojunction detector can be: (i) positioned near active region, (ii) fabricated using optical lithography, (iii) integrated without adversely affecting the time response, suggests possible realization of heterojunction based plasmonic mid-infrared photodetector.

[1]C. C. Chang, Y. D. Sharma, Y. S. Kim, J. A. Bur, R. V. Shenoi, S. Krishna, D. Huang, and S. Y. Lin, Nano Lett. **10**, 1704 (2010).
[2]J. Rosenberg, R. V. Shenoi, T. E. Vandervelde, S. Krishna, and O. Painter, Appl. Phys. Lett. **96**, 161101 (2009).
[3]Z. Yu, G. Veronis, S. Fan, and M. L. Brongersma, Appl. Phys. Lett. **89**, 151116 (2006).
[4]C. Y. Bin, Optics Exp. **17**, 3130 (2009).
[5]H. Li and X. Chenga, J. Vac. Sci. Technol. B **26**, 2156 (2008).
[6]S. G. Matsik, M. B. M. Rinzan, D. G. Esaev, and A. G. U. Perera, Appl. Phys. Lett. **84**, 3435 (2004).
[7]J. Olkkonen, K. Kataja, and D. G. Howe, Optics Exp. **14**, 11506 (2006).
[8]J. A. Shackleford, R. Grote, M. Currie, J. E. Spainer, and Bahram Nabet, Appl. Phys. Lett. **94**, 083501 (2009).
[9]A. P. Hibbins, W. A. Murray, J. Tyler, S. Wedge, W. L. Barnes, and J. R. Sambles, Phys. Rev. B **74**, 073408 (2006).
[10]G. Leveque and O. J. F. Martin, J. Appl. Phys. **100**, 124301 (2006).
[11]J. Lu, C. Petre, E. Yablonovitch, and J. Conway, J. Opt. Soc. Am. B **24**, 2268 (2007).
[12]E. Dupont, J. Appl. Phys. **88**, 2687 (2000).
[13]L. Wendler and T. Kraft, Physica B: Condensed Matter, **271**, 33 (1999).
[14]A. L. Korotkov, A. G. U. Perera, W. Z. Shen, J. Herfort, K. H. Ploog, W. J. Schaff, and H. C. Liu, J. Appl. Phys. **89**, 3295 (2001).
[15]http://www.ioffe.ru/SVA/NSM/Semicond/index.html.
[16]P. Sheng, R. S. Stepleman, and P. N. Sanda, Phys. Rev. B **26**, 2907 (1982).
[17]L. Wendler, T. Kraft, M. Hartung, A. Berger, A. Wixforth, M. Sundaram, J. H. English, and A. C. Gossard, Phys. Rev. B **55**, 2303 (1997).
[18]M. Foresti, L. Menez, and A. V. Tishchenko, J. Opt. Soc. Am. A **23**, 2501 (2006).
[19]A. G. U. Perera, H. X. Yuan, and M. H. Francombe, J. Appl. Phys. **77**, 915 (1995).
[20]D. G. Esaev, M. B. M. Rinzan, S. G. Matsik, and A. G. U. Perera, J. Appl. Phys. **96**, 4588 (2004).
[21]M. R. Gadson, I. R. Hooper, and J. R. Sambles, Optics Exp. **16**, 22003 (2008).
[22]J. Hetterich, G. Bastin, N. A. Gippius, S. G. Tikhodeev, G. Von Plessen, and U. Lemmer, IEEE J. Quantum Electron. **43**, 855 (2007).